Pergamon

1350-4495(94)00099-9

Infrared Phys. Technol. Vol. 36, No. 2, pp. 623–637, 1995

1350-4495/95 $9.50 + 0.00

DIFFRACTION EFFECTS IN IR HALFTONE TRANSPARENCIES

ARNOLD DANIELS,[1] GLENN D. BOREMAN[1] and EYAL SAPIR[2]

[1]Department of Electrical Engineering, Center for Research in Electro-Optics and Lasers (CREOL), University of Central Florida, Orlando, FL 32816 and [2]CI Systems Inc., 5137 Clareton Drive, Suite No. 220, Agoura Hills, CA 91301, U.S.A.

(Received 12 July 1994)

Abstract—Halftone transparencies are a useful tool for performance characterization of IR systems. This paper describes halftone transparencies called thermoscenes, which are lithographically produced patterns of apertures in a metallic coating placed on a transparent IR substrate. To fabricate thermoscene transparencies that are radiometrically accurate, a linear dependence is desired between aperture size and transmittance. We examine the transmittance as a function of hole size for structures suitable for application in halftone transparencies in the 3–5 and 8–12 μm bands in the IR. A theoretical model is developed, based on vector diffraction theory, that agrees with measurements within $\pm 2\%$ for the 3–5 μm and $\pm 3\%$ for 8–12 μm spectral regions. Results are that the transmittance is proportional to the aperture area, for apertures larger than four times the wavelength.

I. INTRODUCTION

The thermoscene[1,2] is an IR halftone transparency that has been developed to simulate various IR scenes. The thermoscene transparency consists of a mesh of variable-sized holes. When this transparency is placed in front of an IR source such as an extended-area blackbody, it simulates a two-dimensional radiant exitance pattern. The thermoscene is made of a metallic deposition on a flat parallel window of IR transmissive material. Using lithographic processes, holes of various sizes are produced on a two-dimensional matrix to make the desired scene pattern.

The thermoscene is important because of its wide range of applications, such as the construction of realistic IR scenes to identify and recognize specific objects in specific environmental conditions, testing of a thermal-imager response to a spatial-contrast vibration of a single frequency component using a thermoscene with a sinusoidal pattern instead of a bar target. A new application being developed consists of tests for modulation transfer function (MTF) using random patterns of known spatial frequency;[3] these random patterns can be transferred on thermoscenes to test MTF for both staring and scanning IR systems. Although this IR transparency has been successfully tested in IR imaging systems,[4] its transmittance effects as a function of wavelength has never been examined. The mathematical formulation of the diffraction effects of the thermoscene is presented and generalized for a thermal imaging system.

With the thermoscene, a variable contrast can be simulated without changing the temperature of the IR source. When the pattern is placed in front of a thermal radiation source, the larger holes transmit more energy than the smaller ones, thus simulating regions of higher and lower temperature or emissivity. We demonstrate here that the power of the radiation transmitted is approximately proportional to the area of the aperture if the aperture size is greater than the light wavelength (λ) used. However for holes smaller than λ, strong diffraction effects are seen and the transmitted radiation is no longer proportional to the area of the hole. Radiometric tests were conducted in the 3–5 μm and 8–12 μm spectral bands using two thermoscenes, which were manufactured having 256 gray levels where each gray level consists of a region of apertures of different sizes. Thus we obtain calibration curves of the transmittance vs aperture area.

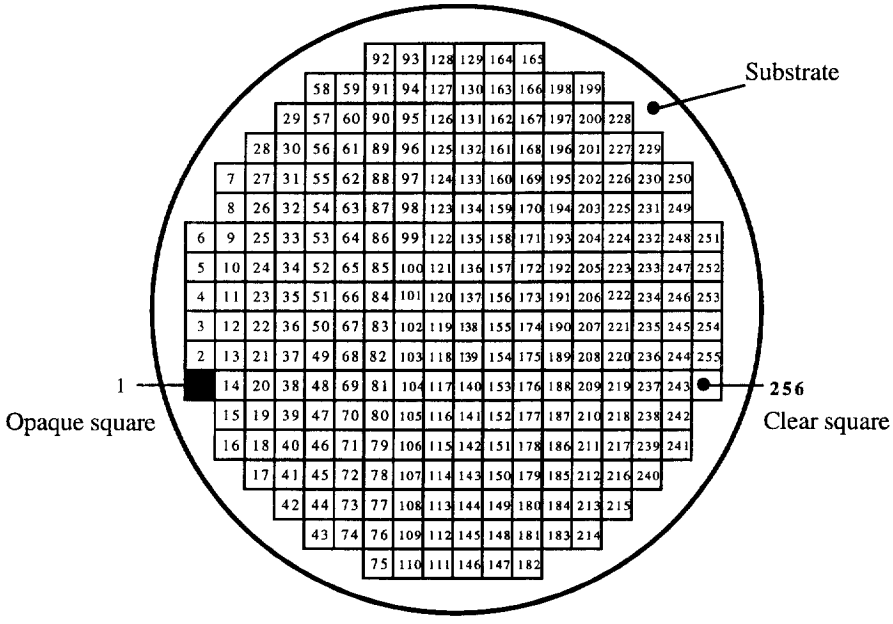

Fig. 1. Structure of the diffraction thermoscene with 256 different gray levels.

The design and optimization of these halftone transparencies are considered to ensure that their smallest holes are within the linear region of the transmittance curves. The diffraction theory for the transmittance of radiation through an array of square apertures on a dielectric slab is derived using vector diffraction theory for comparison.

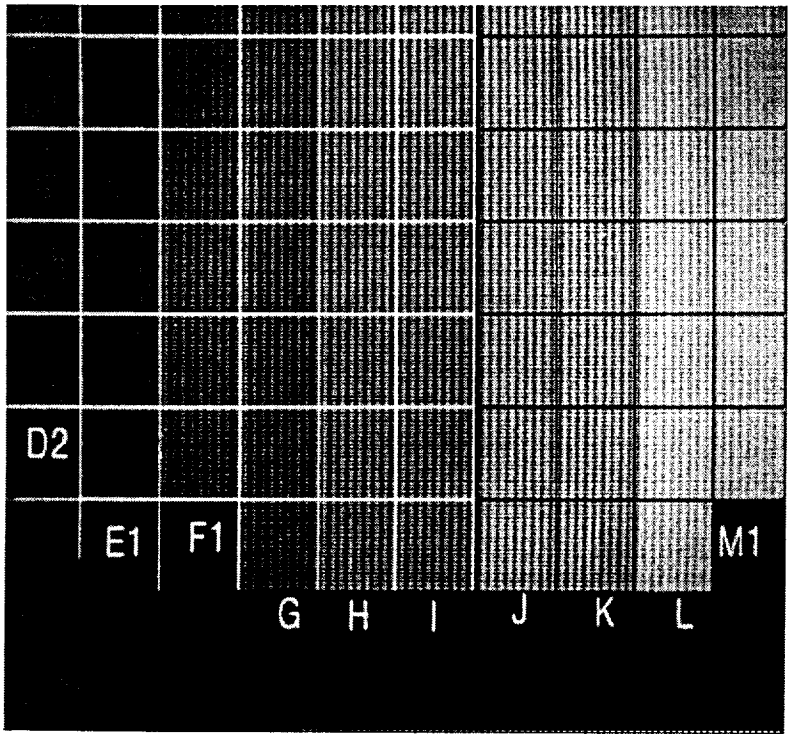

Fig. 2. Magnified image of a section of the thermoscene. The size of each individual square is 2.4 × 2.4 mm.

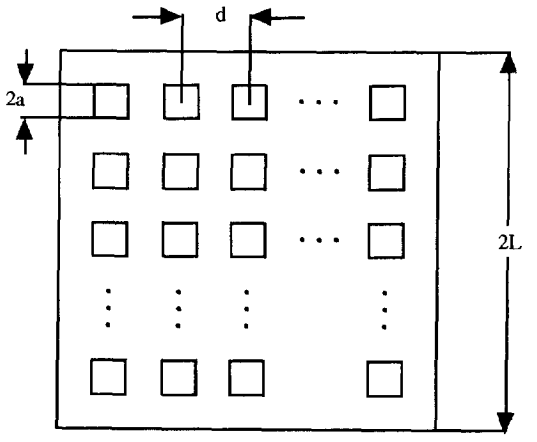

Fig. 3. Array structure of each of the gray levels.

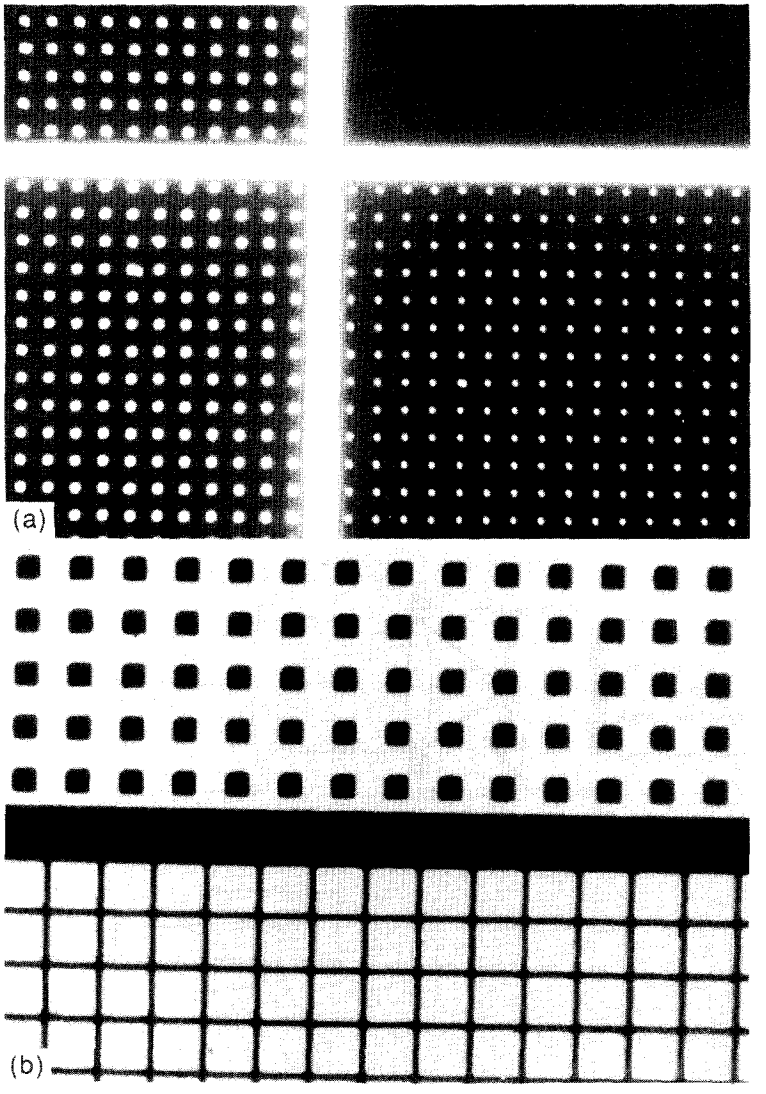

Fig. 4. (a) Magnification of different gray level squares; (b) phase change. The period d in each case is 64.4 μm.

II. THERMOSCENE PROPERTIES

Transmittance vs aperture measurements were performed using two thermoscenes, one on a sapphire (Al_3O_2) substrate and the other on a zinc selenide (ZnSe) substrate. These thermoscenes were manufactured having 256 identically sized square regions, each one corresponding to a different gray level. The structure of these thermoscenes is depicted in Fig. 1.

During the manufacturing process of the diffraction thermoscenes, a layer of chrome was deposited on the IR substrate. The thickness of the metal deposited on the sapphire window was 150 nm. This layer prevents any transmittance through the opaque areas of this thermoscene. The chrome layer applied to the ZnSe substrate was much thinner. Measuring the transmittance of the chrome layer, we calculate a thickness of 12 nm, using the skin-depth theory of Section IV.1. The same theory is used to verify that the transmittance of the chrome deposited on the sapphire window can be neglected because of the thicker coating.

Figure 2 shows a magnified image of the thermoscene, for which the total structure is shown in Fig. 1. Each square region is an array of 38 × 38 square apertures. By varying the aperture size, the 256 different gray levels are achieved. A schematic arrangement of one of these gratings which consists of a periodic transmissive structure on an IR dielectric substrate is shown in Fig. 3. This uniform array of $n \times n$ square elements of size $2a$ are positioned along the x and y directions and separated by a center-to-center distance $d = 64.4\,\mu$m. The total size of the square is $2L = 2.4$ mm. The size of the square apertures is $2a$, and varies linearly 255 times from $2a = 6\,\mu$m (square number 2 in Fig. 1) to $2a = 2L$ (square number 256 in Fig. 1), setting each time a different gray level for each of the 255 squares. The gray level of square number 1 in Fig. 1, consists of chrome coating with no holes in it, setting the floor value for the transmittance.

The microscopic structure of these gratings is shown in Fig. 4, where four different gray levels (squares 1, 2, 13, 14 of Fig. 1) show different arrays with different aperture sizes. Figure 4(b) shows a change of phase that occurs between gray levels 128 and 129. This modification was deliberately performed to avoid lines less than 6 μm, simplifying the construction and handling of the thermoscenes.

The experiments were conducted in the 3–5 μm for the sapphire thermoscene and in the 8–12 μm region using the ZnSe thermoscene.

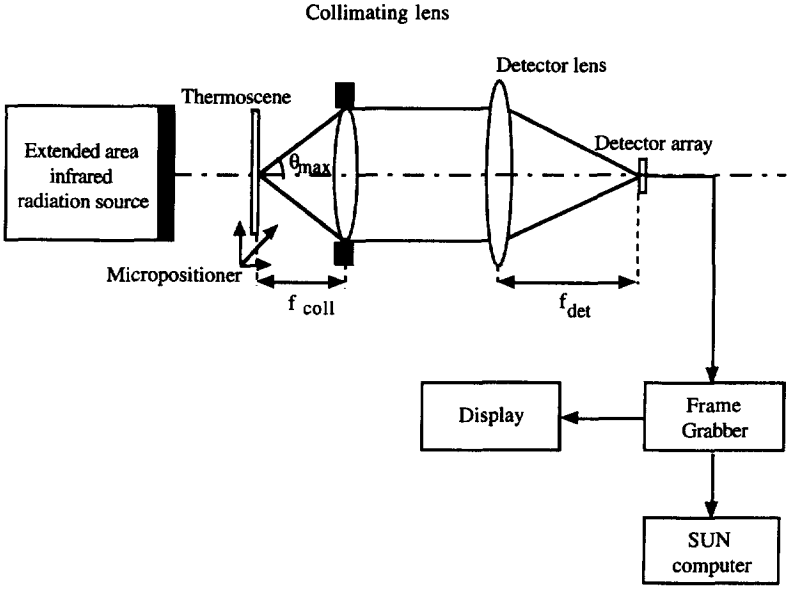

Fig. 5. Transmission experiments setup.

III. MEASUREMENTS OF THE TRANSMISSION LEVELS OF THE THERMOSCENES

The radiometric measurements of the 256 different gray levels were carried out using the setup shown schematically in Fig. 5.

The IR source used is a blackbody with a 102 cm^2 emitting surface set at 100°C. The thermoscene is back illuminated by the blackbody source and imaged on the detector array by a combination of a collimating lens (100 mm focal length, $F/3$) and the detector lens on the IR camera. The detector arrays used in the experiments were a platinum-silicide (PtSi) Schottky-barrier charge coupled device in the 3–5 μm and mercury cadmium telluride (HgCdTe) SPRITE in the 8–12 μm. The detector lenses have $f = 50$ mm for the PtSi system and $f = 109.2$ mm for the HgCdTe system. In each case the collimating lens is the aperture stop for the imaging system.

The diffraction thermoscene was positioned using a multi-axis stage, to align each square under test in the center of the field of view, preventing cosine-to-the-fourth falloff. The image obtained was sufficiently sharp that Moire fringes seen in Fig. 2 appeared in the image because of the periodicity of the pattern of the thermoscene and the detector array; this artifact allowed us to focus the system with high accuracy. The d.c. level and gain of each camera were adjusted to obtain a dynamic range allowing a measurable signal at both floor value (square 1—metallic coating with no holes) and a reference value (square 256—no metallic coating, just the substrate).

The video image is captured by a frame grabber and analyzed to find the average pixel values in the image of the particular square under test. This spatial averaging smooths the Moire fringes. The signal-to-noise ratio (SNR) of the system is improved using temporal averaging, which allows us to measure the transmittance difference between adjacent gray levels. For most of the data sets, five-frame temporal averages were used. For measurements of very low transmittance on the sapphire substrate, 20-frame averages were used. Direct image-data (without averaging) profiles are shown in Fig. 6.

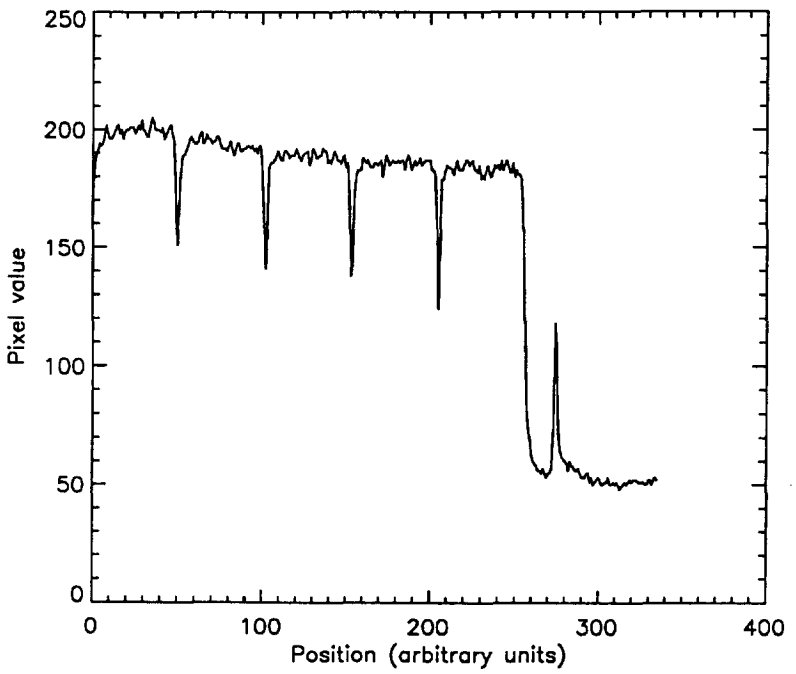

Fig. 6. Signal profiles of adjacent gray levels, without averaging.

The experimental transmittance τ_e is calculated using the following formula:

$$\tau_e = \frac{\text{average pixel value of square under test} - \text{average pixel value of square 1}}{\text{average pixel value of square 256} - \text{average pixel value of square 1}}, \tag{1}$$

which normalizes out both the Fresnel reflection losses in the substrate material and the finite transmittance of the thin chrome coating of the ZnSe thermoscene. Equation (1) yields the transmittance of the metallic mesh of holes, for any given gray level. The transmittance was measured for each of the 256 different squares. Results are presented in Section V.

IV. THEORETICAL MODEL

We use vector diffraction theory,[5–7] to develop a model for the transmittance of the thermoscene that is valid for aperture sizes equal to or greater than the wavelength.

We calculate the skin depth of an electromagnetic wave in the metallic chrome coating of the thermoscene. We also calculate the diffraction of electromagnetic waves for the special case of a thin, perfectly conducting, plane screen with a square aperture. This special case is then generalized for the thermoscene mesh, where the transmittance of an incoherent field through an array of square apertures in an infrared substrate is derived.

1. Skin depth of an electromagnetic wave in the chrome

Considering an isotropic medium of dielectric constant ϵ, permeability μ, and conductivity σ, the distance the wave must travel in a lossy medium to reduce its value to $e^{-1} = 36.8\%$ is defined as the skin depth or penetration depth (δ).[5,8,9] This distance is defined as

$$\delta = \frac{1}{\alpha} = \frac{1}{2\pi\nu\sqrt{\mu\epsilon}\left\{\frac{1}{2}\left[\sqrt{1+\left(\frac{\sigma}{2\pi\nu\epsilon}\right)^2}-1\right]\right\}^{1/2}}, \tag{2}$$

where α is the attenuation constant and ν is the optical frequency. The chrome is a very good conductor, so that the attenuation constant in equation (2) can be written using the binomial expansion:

$$\alpha = 2\pi\nu\sqrt{\mu\epsilon}\left\{\frac{1}{2}\left[\sqrt{1+\left(\frac{\sigma}{2\pi\nu\epsilon}\right)^2}-1\right]\right\}^{1/2}, \tag{3a}$$

$$\alpha = 2\pi\nu\sqrt{\mu\epsilon}\left\{\frac{1}{2}\left[\frac{\sigma}{2\pi\nu\epsilon}+\frac{1}{2}\frac{2\pi\nu\epsilon}{\sigma}-\frac{1}{8}\left(\frac{2\pi\nu\epsilon}{\sigma}\right)^3+\cdots-1\right]\right\}^{1/2}. \tag{3b}$$

Retaining only the first term of the infinite-series expansion, the skin depth defined in equation (2) can be approximated for a conductor by

$$\delta = \sqrt{\frac{1}{\pi\mu\sigma\nu}}. \tag{4}$$

Defining t as the thickness of a chrome layer deposited on an IR substrate, the ratio of the transmitted power to the incident power called transmittance coefficient τ_{chrome} is calculated by

$$\tau_{\text{chrome}} = \frac{\phi_{\text{trans}}}{\phi_{\text{inc}}} = \left(\frac{1}{e}\right)^{2t/\delta}, \tag{5}$$

where ϕ_{trans} is the transmitted power and ϕ_{inc} is the incident power at $t = 0$.

The chrome thickness on the sapphire substrate is $t = 150$ nm. The electrical conductivity and the magnetic permeability of the chrome were adapted from the CRC handbook[10] to be $\sigma = 7.87 \times 10^6$ Siemens and $\mu = 1.257 \times 10^{-6}$ H/m, respectively. The skin depth and the

transmittance of the chrome deposited on this particular window are evaluated using equations (4) and (5) and $\lambda = 4\,\mu$m yielding $\delta = 20.71$ nm, and $\tau = 5.12 \times 10^{-5}\%$. Thus a negligible per cent of power is transmitted through the chrome and can be ignored. Therefore the screen of the sapphire substrate can be considered opaque (i.e. a perfectly conducting screen) except for the open apertures.

In the case of the ZnSe diffraction thermoscene, a transmittance of the chrome layer measured with a FTIR spectrophotometer is 10% at $\lambda = 4\mu$m. The thickness of the chrome layer was then calculated using equation (5) to be 12.7 nm. This thin chrome layer deposition was an error during the manufacturing process of this particular thermoscene, which changed the floor value for the radiometric measurements. Using equation (1), this fixed offset is corrected for automatically.

2. Transmittance by a single aperture

We proceed to calculate the transmitted power of a single square aperture in an opaque screen, which will be used to derive the mathematical model of the thermoscene arrays and of the overall thermal-imaging system.

For a plane surface the vector expression of the diffracted electric field is given by[5]

$$\mathbf{E}(\mathbf{x}) = j\frac{e^{jkr}}{2\pi r}\,\mathbf{k} \times \int_{\text{Aperture}} \hat{\mathbf{n}} \times \mathbf{E}(\mathbf{x}')e^{-j(\mathbf{k}\cdot\mathbf{x}')}\,da', \tag{6}$$

where the integration is performed over a square aperture in a perfectly conducting screen. $\mathbf{E}(\mathbf{x}')$ is the tangential electric field in the opening which is the incident unperturbed field. The variable $\mathbf{x}' = x'\hat{x} + y'\hat{y}$ represents the coordinates of the element of the surface da', and r is the length of the vector $\mathbf{x}$ from the origin O to the observation point P. The vector $\hat{\mathbf{n}}$ is the unit normal to the surface da', and $\mathbf{k}$ is the diffracted wave vector in the direction of the observation point and is given by

$$\mathbf{k} = |\mathbf{k}|\frac{\mathbf{x}}{r} = k\frac{x\hat{\mathbf{x}} + y\hat{\mathbf{y}} + z\hat{\mathbf{z}}}{\sqrt{x^2 + y^2 + z^2}}, \tag{7}$$

where k is the wave number, $(k = 2\pi/\lambda)$.

The coordinate system used is shown in Fig. 7. Here we consider a plane wave at normal incidence to the screen with a square hole of side $2a$. The wave is incident from the $z < 0$ side, in which case the domain $z > 0$ is the region of the diffraction fields.

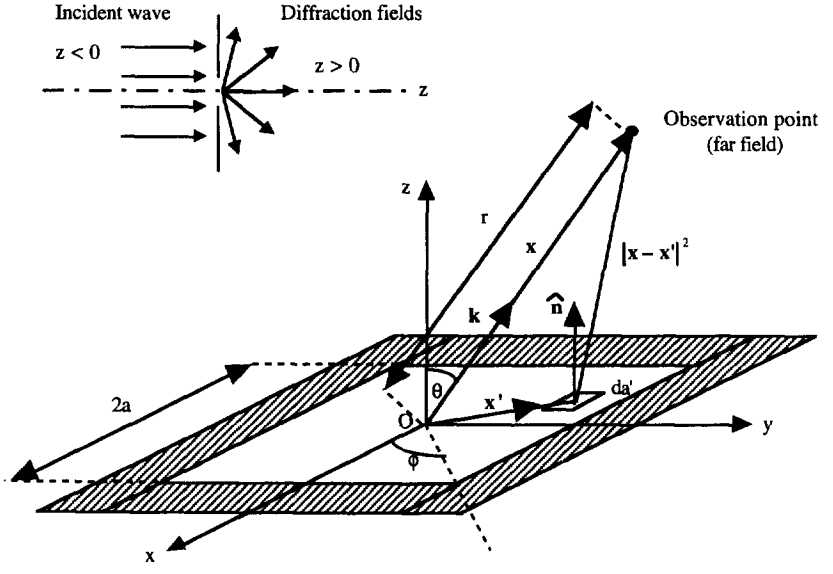

Fig. 7. Transmittance by a square aperture with side length $2a$. Insert: Configuration of incident and diffraction radiation.

We proceed now to solve equation (6). Taking the dot product between the vectors $\mathbf{k}$ and $\mathbf{x}'$

$$\mathbf{k}\cdot\mathbf{x}' = \frac{|k|}{\sqrt{x^2+y^2+z^2}}(x\hat{\mathbf{x}}+y\hat{\mathbf{y}}+z\hat{\mathbf{z}})\cdot(x'\hat{\mathbf{x}}+y'\hat{\mathbf{y}}), \tag{8a}$$

yielding

$$\mathbf{k}\cdot\mathbf{x}' = |k|\frac{(x'x+y'y)}{\sqrt{x^2+y^2+z^2}}. \tag{8b}$$

The plane wave propagates in the z direction, therefore the electric-field component in this direction is zero. Assuming for convenience that the electric field is linearly polarized in the x direction, the cross product between $\hat{\mathbf{n}}$ and $\mathbf{E}(\mathbf{x}')$ at $z=0$ is calculated as

$$\hat{\mathbf{n}}\times\mathbf{E}(x') = \mathsf{E}_0(\hat{\mathbf{z}}\times\hat{\mathbf{x}}) = \mathsf{E}_0\hat{\mathbf{y}}. \tag{9}$$

Substituting equations (7), (8b), and (9) into equation (6) we obtain

$$\mathbf{E}(x,y,z) = j\frac{e^{jkr}}{2\pi r}|k|\frac{x\hat{\mathbf{x}}+y\hat{\mathbf{y}}+z\hat{\mathbf{z}}}{\sqrt{x^2+y^2+z^2}}\times\int_{\text{Aperture}}\mathsf{E}_0\hat{\mathbf{y}}\exp\left(-jk\frac{xx'+yy'}{\sqrt{x^2+y^2+z^2}}\right)dx'\,dy', \tag{10a}$$

$$\mathbf{E}(x,y,z) = j\,\mathsf{E}_0\frac{e^{jkr}}{2\pi r}|k|\frac{(x\hat{\mathbf{z}}-z\hat{\mathbf{x}})}{\sqrt{x^2+y^2+z^2}}\int_{-a}^{a}\int_{-a}^{a}\exp\left(-jk\frac{xx'+yy'}{\sqrt{x^2+y^2+z^2}}\right)dx'\,dy'. \tag{10b}$$

Solving equation (10b) gives

$$\mathbf{E}(x,y,z) = j2\mathsf{E}_0\frac{e^{jkr}}{k\pi}\frac{(z\hat{\mathbf{x}}-x\hat{\mathbf{z}})}{xy}\sin\left(\frac{|k|ax}{\sqrt{x^2+y^2+z^2}}\right)\sin\left(\frac{|k|ay}{\sqrt{x^2+y^2+z^2}}\right). \tag{11}$$

Assuming that we are operating in the far-field region [Fraunhofer approximation[6,8,11]] $z \gg x, y$, equation (11) becomes

$$\mathbf{E}(x,y,z) = \hat{\mathbf{x}}j2\mathsf{E}_0\frac{e^{jkr}}{k\pi}\frac{z}{xy}\sin\left(\frac{|k|ax}{r}\right)\sin\left(\frac{|k|ay}{r}\right). \tag{12}$$

Introducing plane polar coordinates in equation (12)

$$\mathbf{E}_{\text{polar}}(r,\theta,\varphi) = j2\mathsf{E}_0\frac{e^{jkr}}{k\pi r}\frac{(\hat{\boldsymbol{\theta}}\cos\theta\cos\varphi-\hat{\boldsymbol{\varphi}}\sin\varphi)\cos\theta}{\sin^2\theta\sin\varphi\cos\varphi}\sin(ka\sin\theta\cos\varphi)\sin(ka\sin\theta\sin\varphi). \tag{13}$$

The diffracted irradiance on a spherical surface from a single aperture (E_{sphere}) is shown in Fig. 8 and is calculated taking the squared magnitude of the diffracted electric field at the surface of the sphere $E_{\text{sphere}} = |\mathbf{E}_{\text{polar}}|^2$ yielding

$$E_{\text{sphere}} = \frac{4E_0}{(k\pi r)^2}\frac{(\cos^2\theta\cos^2\varphi+\sin^2\varphi)\cos^2\theta}{\sin^4\theta\sin^2\varphi\cos^2\varphi}\sin^2(ka\sin\theta\cos\varphi)\sin^2(ka\sin\theta\sin\varphi), \tag{14}$$

where $E_0 = |\mathsf{E}_0|^2$ is the incoming irradiance in W/cm^2 that falls on the aperture at $z=0$ (see Fig. 8) from the blackbody, defined as

$$E_0 = \epsilon_{gb}\frac{c_1}{\lambda^5}\frac{d\lambda}{e^{c_2/\lambda T}-1}, \tag{15}$$

where $c_1 = 2\pi hc^2 = 3.74\times10^{-12}$ Wcm^2, $c_2 = hc/k' = 1.434$ Kcm, h is Planck's constant ($h = 6.6262\times10^{-34}$ J/s), k' is Boltzmann's constant ($k' = 1.38\times10^{-23}$ J/K), c is the speed of light in vacuum ($c = 3\times10^{10}$ cm/s), T is the temperature at which the blackbody was set in the experiment ($T = 100$°C), ϵ_{gb} is the emissivity of the blackbody (actually a graybody with $\epsilon_{\text{gb}} = 0.97$), and λ is the wavelength.

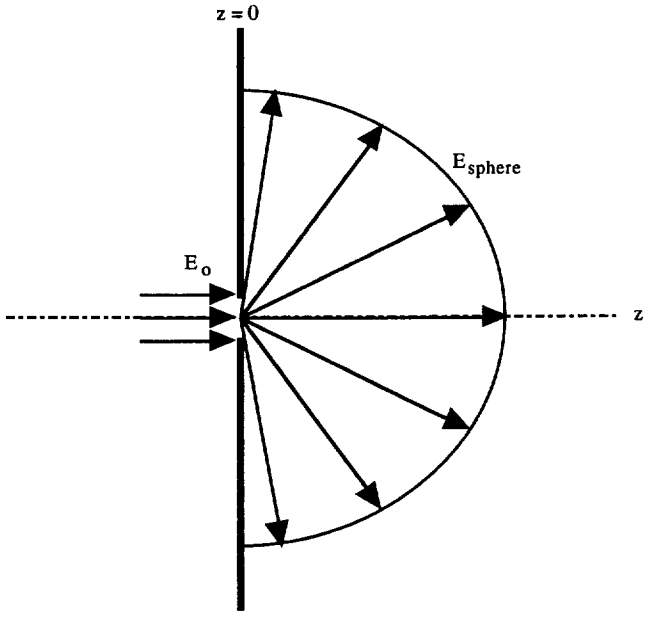

Fig. 8. The irradiance of a thermoscene array radiating into hemisphere.

Defining intermediate variables

$$\eta = \cos^2\theta \cos^2\varphi + \sin^2\varphi, \tag{16a}$$

$$\psi = \sin^4\theta \sin^2\varphi \cos^2\varphi, \tag{16b}$$

$$\beta = \sin\theta \cos\varphi, \tag{16c}$$

$$\gamma = \sin\theta \sin\varphi. \tag{16d}$$

Equation (14) can be written as

$$E_{\text{sphere}} = \frac{4E_0}{(k\pi r)^2}\frac{\eta}{\psi}\cos^2\theta \sin^2(ka\beta)\sin^2(ka\gamma). \tag{17}$$

The total transmitted power that is radiated from a single aperture is obtained by integrating equation (17) over the entire hemisphere area (see Fig. 8) giving

$$\phi_{\text{aperture}} = \frac{4E_0}{(\pi kr)^2}\int_{\varphi=0}^{2\pi}\int_{\theta=0}^{\pi/2}\frac{\eta}{\psi}\cos^2\theta \sin^2(ka\beta)\sin^2(ka\gamma)r^2\sin\theta \, d\theta \, d\varphi. \tag{18}$$

Defining $\phi_i = 4a^2E_0$ as the total power incident on the aperture, the ratio of transmitted power to incident power of the square aperture defines the transmittance τ_{aperture} and is given by

$$\tau_{\text{aperture}} = \frac{\phi_{\text{aperture}}}{\phi_i} = \frac{1}{(\pi ka)^2}\int_{\varphi=0}^{2\pi}\int_{\theta=0}^{\pi/2}\frac{\eta}{\psi}\cos^2\theta \sin^2(ka\beta)\sin^2(ka\gamma)\sin\theta \, d\theta \, d\varphi, \tag{19}$$

which is a function of wavelength because $k = 2\pi/\lambda$.

A plot of transmittance (τ_{aperture}) vs aperture size normalized to wavelength ($2a/\lambda$) is shown in Fig. 9. This plot was numerically calculated from equation (19). It can be seen that if the opening is twice the wavelength or larger ($2a/\lambda \geqslant 2$), the pattern transmission is greater than 95%, which means that the main part of the wave passes through the opening in the manner of geometrical optics. For $2a/\lambda = 1$, the transmitted wave starts to be distributed in different directions from the incident relation (i.e. diffraction effects occur), and the transmittance coefficient decreases to 85%.

When the aperture is much smaller than the wavelength ($2a/\lambda \ll 1$), the transmitted power is strongly diffracted, and the transmittances decreases further.

The diffraction from a single square aperture (for the case $2a/\lambda \geqslant 1$) varies as a function of wavelength when a normally incident plane wave strikes the aperture, as this selection describes. The diffraction of electromagnetic radiation by a hole that is small compared with the wavelength is given by Morse,[12] Stratton[13] and Bethe.[14] However our main concern in this paper is to determine the minimum aperture size to avoid diffraction-induced nonlinearity of transmittance in the fabrication of the thermoscene. Therefore, for this application, the equations developed in this section are totally valid, because $2a/\lambda > 1$.

3. Calculation of array transmittance

The thermoscene in the system of Fig. 5 is illuminated by the incoherent source of radiation (i.e. an extended-source blackbody). For this type of illumination, the E field amplitudes at all points are statistically independent.[6,15] When the transmitted radiation from the different square apertures in the array are superimposed, no interference is observed. The schematic arrangement of the periodic grating is shown in Fig. 3, where each represents a different gray level in the thermoscene.

Thus the total transmitted power of the array ϕ_{array} is the power contribution of each of its individual apertures, yielding

$$\phi_{\text{array}} = n^2 \phi_{\text{aperture}}, \tag{20}$$

where n^2 is the total number of individual elements and ϕ_{aperture} is the diffracted power of a single element of the array of area $4a^2$ given by equation (18). Substituting equation (18) into equation (20) yields

$$\phi_{\text{array}} = \frac{4n^2 E_0}{(\pi k r)^2} \int_{\varphi=0}^{2\pi} \int_{\theta=0}^{\pi/2} \frac{\eta}{\psi} \cos^2\theta \sin^2(ka\beta)\sin^2(ka\gamma) r^2 \sin\theta \, d\theta \, d\varphi. \tag{21}$$

Equation (21) is the total transmitted power that is radiated from one of the arrays of the thermoscene over the entire hemisphere area. However in our measurements the collected power

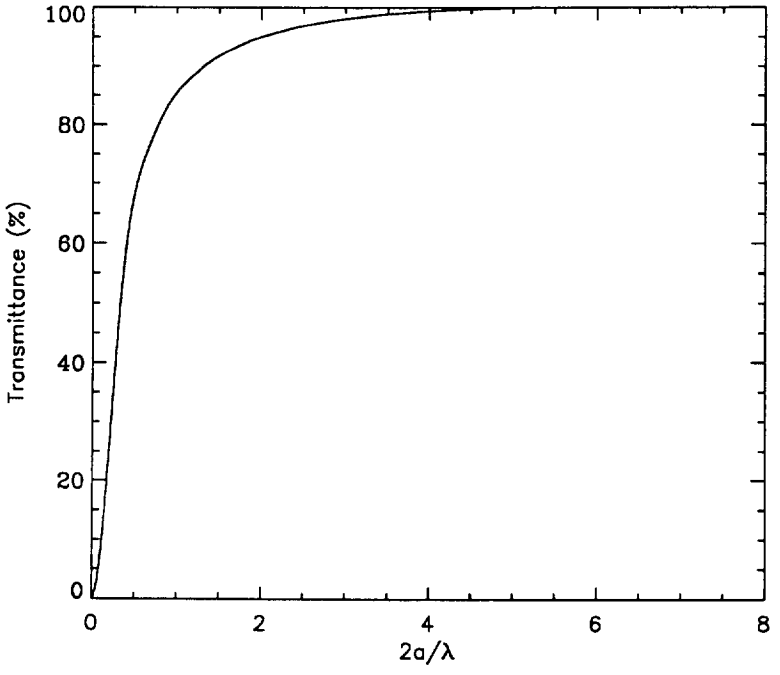

Fig. 9. Transmittance dependence of a single aperture as a function of $2a/\lambda$.

is limited by the aperture stop of the imaging system of Fig. 5. This amount of collected power is then incident on the detector array, which operates in a specific spectral region. In addition to that, the in-band transmittance of the substrate (τ_{subs}), optics (τ_{opt}), and atmosphere (τ_{atm}), must also be considered.

To fulfill these conditions, equation (21) is multiplied by τ_{subs}, τ_{opt} and τ_{atm}, respectively, and is integrated over the collecting optics area and over the desired spectral region, yielding

$$\phi_{collected} = \frac{\epsilon_{gb} n^2 c_1 \tau_{subs} \tau_{opt} \tau_{atm}}{\pi^4 f_{coll}^2} \int_{\lambda_1}^{\lambda_2} \frac{1}{\lambda^3 [\exp(c_2/\lambda T) - 1]} \times \int_{\varphi=0}^{2\pi} \int_{\theta=0}^{\theta_{max}} \frac{\eta}{\psi} \cos^2\theta \sin^2\left(\frac{2\pi}{\lambda} a\beta\right) \sin^2\left(\frac{2\pi}{\lambda} a\gamma\right) f_{coll}^2 \sin\theta \, d\theta \, d\varphi \, d\lambda, \quad (22)$$

where θ_{max} is the marginal ray angle (see Fig. 5), and E_0 has been substituted using equation (15). The distance r in equation (21) has been replaced by the focal length of the collimating optics (f_{coll}). Equation (22) calculates the power collected from a particular gray-level array of the thermoscene.

Next we calculate the collected power that strikes the detector when the gray level under test is the clear square of size $2L$ (see Fig. 1), which corresponds to the reference value. This normalizes the systematic losses of the system as in equation (1).

This reference power is calculated using the same principles as in equation (22) yielding

$$\phi_{ref} = \frac{\epsilon_{gb} c_1 \tau_{subs} \tau_{opt} \tau_{atm}}{\pi^4 f_{coll}^2} \int_{\lambda_1}^{\lambda_2} \frac{1}{\lambda^3 [\exp(c_2/\lambda T) - 1]} \times \int_{\varphi=0}^{2\pi} \int_{\theta=0}^{\theta_{max}} \frac{\eta}{\psi} \cos^2\theta \sin^2\left(\frac{2\pi}{\lambda} L\beta\right) \sin^2\left(\frac{2\pi}{\lambda} L\gamma\right) f_{coll}^2 \sin\theta \, d\theta \, d\varphi \, d\lambda, \quad (23)$$

where the size of the diffracting aperture is taken to be the size of the reference cell ($2L$).

To calculate the amount of detector response expected from equations (22) and (23), the detector spectral responsivity $R(\lambda)$ must be included. The detector outputs in volts of the array under test and of the reference value are then given by

$$V_{array} = \frac{\epsilon_{gb} n^2 c_1 \tau_{subs} \tau_{opt} \tau_{atm}}{\pi^4} \int_{\lambda_1}^{\lambda_2} \frac{R(\lambda)}{\lambda^3 [\exp(c_2/\lambda T) - 1]} \times \int_{\varphi=0}^{2\pi} \int_{\theta=0}^{\theta_{max}} \frac{\eta}{\psi} \cos^2\theta \sin^2\left(\frac{2\pi}{\lambda} a\beta\right) \sin^2\left(\frac{2\pi}{\lambda} a\gamma\right) \sin\theta \, d\theta \, d\varphi \, d\lambda, \quad (24)$$

and

$$V_{ref} = \frac{\epsilon_{gb} c_1 \tau_{subs} \tau_{opt} \tau_{atm}}{\pi^4} \int_{\lambda_1}^{\lambda_2} \frac{R(\lambda)}{\lambda^3 [\exp(c_2/\lambda T) - 1]} \times \int_{\varphi=0}^{2\pi} \int_{\theta=0}^{\theta_{max}} \frac{\eta}{\psi} \cos^2\theta \sin^2\left(\frac{2\pi}{\lambda} L\beta\right) \sin^2\left(\frac{2\pi}{\lambda} L\gamma\right) \sin\theta \, d\theta \, d\varphi \, d\lambda, \quad (25)$$

respectively. The spectral responsivities of the PtSi and HgCdTe detectors were supplied on request by Mitsubishi Electric Corporation[16] and Magnavox Electronic Systems Company.[17]

The overall transmittance of the entire system ($\tau_{measured}$) is calculated dividing equation (24) by equation (25) yielding

$$\tau_{measured} = \frac{n^2 \int_{\lambda_1}^{\lambda_2} \frac{R(\lambda)}{\lambda^3[\exp(c_2/\lambda T)-1]} \int_{\varphi=0}^{2\pi} \int_{\theta=0}^{\theta_{max}} \frac{\eta}{\psi} \cos^2\theta \sin^2\left(\frac{2\pi}{\lambda} a\beta\right) \sin^2\left(\frac{2\pi}{\lambda} a\gamma\right) \sin\theta \, d\theta \, d\varphi \, d\lambda}{\int_{\lambda_1}^{\lambda_2} \frac{R(\lambda)}{\lambda^3[\exp(c_2/\lambda T)-1]} \int_{\varphi=0}^{2\pi} \int_{\theta=0}^{\theta_{max}} \frac{\eta}{\psi} \cos^2\theta \sin^2\left(\frac{2\pi}{\lambda} L\beta\right) \sin^2\left(\frac{2\pi}{\lambda} L\gamma\right) \sin\theta \, d\theta \, d\varphi \, d\lambda} \quad (26)$$

Equation (26) is solved numerically for the corresponding spectral region, when varying the aperture size from zero to 64.4 μm (i.e. the distance d in Fig. 3). These theoretical data are presented and compared with the experimental results in the next section.

V. COMPARISON BETWEEN THE THEORETICAL AND EXPERIMENTAL RESULTS

Measurements of transmittance vs aperture area were performed in the 3–5 μm band for the sapphire thermoscene and in the 8–12 μm band for the ZnSe thermoscene. Equation (26) was solved numerically to obtain the theoretical results, and the experimental data were obtained using equation (1). Comparison between the theoretical and experimental results in the 3–5 and 8–12 μm regions are shown in Figs 10 and 11, respectively.

These curves show the dependence of the transmittance as a function of hole size. The experimental data are represented by rhomboids in the 3–5 μm region and stars in the 8–12 μm region. The solid line represents the theoretical curve from equation (26), and the dashed line shows the geometrical-optics limit of transmittance proportional to the aperture area. For the data of Fig. 10 where the aperture area is less than 400 μm^2, we use 20-frame averages to increase the SNR. For all other data, five-frame averages were used.

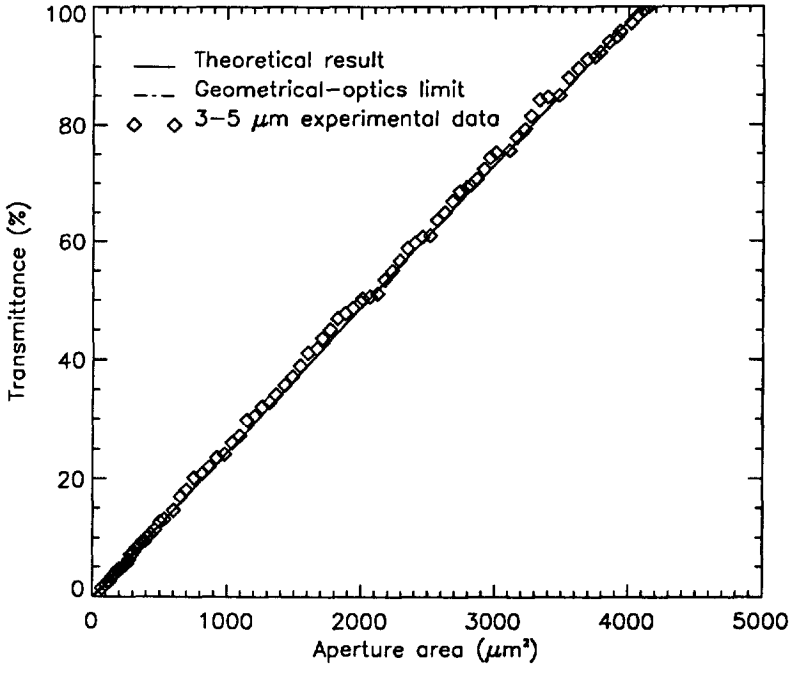

Fig. 10. Transmittance vs aperture area for sapphire thermoscene (3–5 μm).

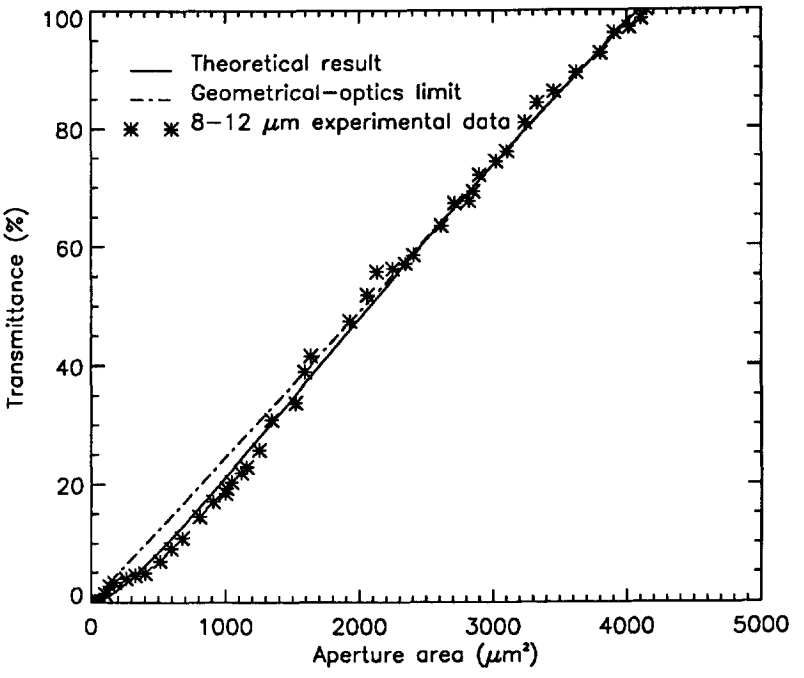

Fig. 11. Transmittance vs aperture area for ZnSe thermoscene (8–12 μm).

The differences in value between the experimental data and the theoretical curve are the result of several sources of error generated by the experimental setup of Fig. 5. These errors were primarily caused by the noise in the electronic system, cooler-cycle-induced variations, temperature fluctuations in the optics train, or by variations in the centering of each thermoscene measurement. These random errors were quantified by calculating the standard deviation of the data points with

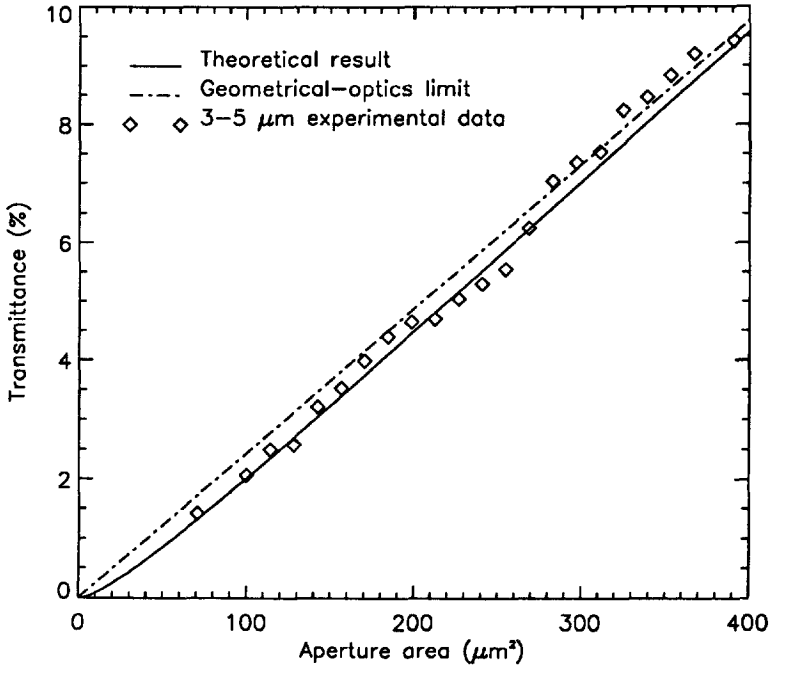

Fig. 12. Small-aperture portion of Fig. 10.

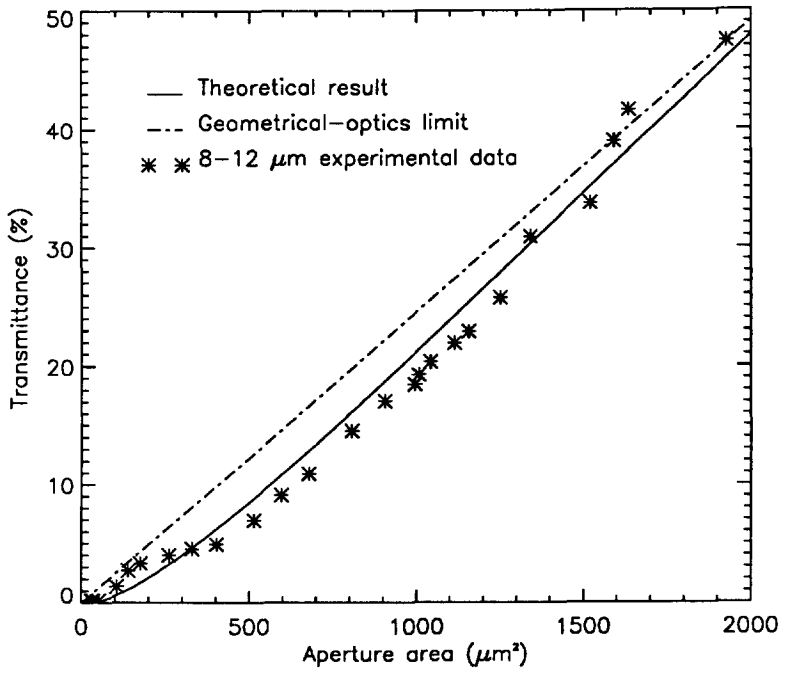

Fig. 13. Small-aperture portion of Fig. 11.

respect to the theoretical curve. The amount of error was calculated to be $\pm 2\%$ for the 3–5 μm spectral band and $\pm 3\%$ for the 8–12 μm spectral band.

Figures 12 and 13 are enlargement of Figs 10 and 11, and show the small-aperture portions of the curves. As we can see from these curves, the transmittance starts to be proportional to the aperture area at 250 μm^2 for the 3–5 μm band and 1500 μm^2 for the 8–12 μm band. Therefore to avoid the nonlinear dependence of transmittance on the aperture area, a minimum aperture size of around 16 μm for 3–5 μm systems and around 40 μm for 8–12 μm systems is required. The relative difference between the geometrical-optics limit and the theoretical diffraction curve at these points are 5.6 and 5.9% for the 3–5 and 8–12 μm regions, respectively.

A rule of thumb can thus be stated:

> "To avoid diffraction-induced nonlinearities of transmittance the minimum aperture size in the design of a thermoscene, must be four times the light wavelength."

VI. CONCLUSIONS

Calibration curves of transmittance vs aperture size were obtained for the proper design and optimization of IR halftone transparencies called thermoscenes. Diffraction effects are avoided when the aperture sizes of these thermoscenes are larger than four times the wavelength of incident radiation, ensuring a linear dependence between the transmittance and the aperture area.

The experiments were performed using thermoscenes with 256 different gray levels, in which these levels consist of periodic screens of different aperture sizes. A mathematical model was formulated using vector diffraction theory, to demonstrate the reliability of the experimental results. Comparison between the theoretical and experimental results show agreement within $\pm 2\%$ for the 3–5 μm spectral band and $\pm 3\%$ for the 8–12 μm spectral band.

The minimum aperture size used in the thermoscene impacts the lithographic precision required in the fabrication process. The aperture dimensions used for the first few gray levels should be as small as possible, within the constraint of transmittance linearity. This leaves more aperture area

(out of the limit of the pixel spacing) to be distributed among the remaining gray levels, which allows the area increment between the successive gray levels to be larger. This eases the resolution requirements in the fabrication process, and as well provides a larger dynamic range of flux values in the scene created.

Acknowledgement—We would like to express our appreciation to CI Systems Inc. for participating in and sponsoring this reasearch.

REFERENCES

1. S. Ghilai, U. Gera, D. Cabib, A. Lapin and Y. Liran, *Proc. Soc. Photo-opt. Instrum. Engrs* **819,** 80 (1987).
2. D. Cabib, J. Eliason, S. Guilai and R. Bracha, *Proc. Soc. Photo-opt. Instrum. Engrs* **1762,** 41 (1992).
3. A. Daniels, G. D. Boreman and A. D. Ducharme, *Proc. Soc. Photo-opt. Instrum. Engrs* **1969,** 20 (1992).
4. A. Daniels, The Thermoscene a Basic Component of Infrared Simulation. Master Thesis, University of Tel-Aviv, Israel (1989).
5. J. D. Jackson, *Classical Electrodynamics*, pp. 298 and 427. John Wiley, New York (1975).
6. J. W. Goodman, *Introduction to Fourier Optics*, Chaps 3, 4, and 6. McGraw-Hill, New York (1968).
7. E. Wolf and E. W. Marchand, *J. Opt. Soc. Am.* **54,** 587 (1964).
8. M. Born and E. Wolf, *Principles of Optics*, p. 614. Pergamon Press, Oxford (1980).
9. C. A. Balanis, *Advanced Engineering Electromagnetics*, p. 149. John Wiley, New York (1989).
10. D. R. Lide, *CRC Handbook of Chemistry and Physics*, pp. 9–33, 12–33, 12–119. CRC The Chemical Rubber Publishing Company, Boca Raton, FL (1991–1992).
11. R. B. Hoover and F. S. Harris Jr, *Oppl. Opt.* **8,** 2161 (1969).
12. P. M. Morse and P. J. Rubinstein, *Phys. Rev.* **54,** 895 (1938).
13. J. A. Stratton and L. J. Chu, *Phys. Rev.* **56,** 99 (1939).
14. H. A. Bethe, *Phys. Rev.* **66,** 163 (1944).
15. R. J. Glauber, *Phys. Rev.* **131,** 2766 (1963).
16. Mike Mays, Mitsubishi Electric Corporation, Torrance, CA. Private communication.
17. Richard Leftwich, Magnavox Electric Systems Company (Electro-Optical System Division) Mahwah NJ. Private communication.